Simultaneous 10 kHz TPIV, OH PLIF, and CH$_2$O PLIF measurements of turbulent flame structure and dynamics

Jeffrey R. Osborne · Sarah A. Ramji · Campbell D. Carter · Scott Peltier · Stephen Hammack · Tonghun Lee · Adam M. Steinberg

Abstract Simultaneous 10 kHz repetition-rate tomographic particle image velocimetry (TPIV), hydroxyl planar laser induced fluorescence (OH PLIF), and formaldehyde (CH$_2$O) PLIF were used to study the structure and dynamics of turbulent premixed flames. The flames investigated span from the classically defined corrugated flamelet regime to conditions at which broadened and/or broken flamelets are expected. Methods are presented for determining 3D flame topologies from the Mie scattering tomography and for tracking features through space and time using theoretical Lagrangian particles. Substantial broadening of the CH$_2$O region is observed with increasing turbulence intensity. However, OH production remains rapid and the region of OH and CH$_2$O overlap remains thin. Local flame speeds exceeding three times the laminar flame speed are observed in regions of flame-flame interaction. Furthermore, a method of tracking fluid residence time within the CH$_2$O layer is presented and shows that residence time decreases at higher turbulence intensity despite the broader distribution of the CH$_2$O, indicating an increase in local reaction rate.

J. R. Osborne, S. A. Ramji, and A. M. Steinberg
University of Toronto Institute for Aerospace Studies
Toronto, Canada
E-mail: josborne@utias.utoronto.ca
sramji@utias.utoronto.ca
adam.steinberg@utoronto.ca
C. D. Carter and S. Peltier
Air Force Research Laboratory
Wright-Patterson Air Force Base, OH, USA
E-mail: campbell.carter@us.af.mil
scott.peltier.5@us.af.mil
S. Hammack and T. Lee
Department of Mechanical Science and Engineering
University of Illinois at Urbana-Champaign, IL, USA
E-mail: shammac2@illinois.edu
tonghun@illinois.edu

1 Introduction

Current gaps in the understanding of turbulent premixed combustion hinder the accuracy and reliability of simulations, particularly for conditions relevant to aerospace propulsion systems (Echekki and Mastorakos, 2010). A primary goal is understanding the interaction between local reaction rate, flame structure, flame topology, and turbulence at such conditions. Development of physics-based combustion models for these processes can greatly benefit from direct experimental measurement, which requires the use of time-resolved, multi-dimensional, and multi-parameter diagnostics. In particular, velocity measurements must be combined with sufficient scalar data to simultaneously describe the turbulence, flame structure, and their interaction.

This paper presents results from simultaneous 10 kHz repetition-rate tomographic particle image velocimetry (TPIV), hydroxyl planar laser induced fluorescence (OH PLIF), and formaldehyde (CH$_2$O) PLIF measurements in a series of turbulent premixed flames at various turbulence intensities, all made using diode-pumped solid-state (DPSS) lasers. The purpose of the paper is to demonstrate and assess the diagnostics, present several analysis techniques that can be applied to such data, and illustrate important combustion phenomena that can thus be quantified.

Planar two- and three-component (i.e. stereoscopic) PIV are common means of measuring velocity fields in reacting and non-reacting flows (Westerweel et al., 2013;

Schroeder and Willert, 2008). However, the 3D nature of turbulent flows means that planar measurements are incapable of fully capturing the flow behavior, e.g. the nine components of the velocity gradient tensor. Additional problems can occur if planar measurements are used to study temporally evolving phenomena, as 3D convection can greatly influence interpretation (Steinberg and Driscoll, 2009; Ganapathisubramani et al., 2008). Several 3D velocimetry techniques have been developed, with TPIV emerging as a popular means of obtaining high-quality measurements in a variety of flows (Elsinga et al., 2006; Elsinga and Ganapathisubramani, 2012), having been applied to, for example, turbulent boundary layer/shock wave interactions (Humble et al., 2009), or vorticity generation in a cylindrical wake (Scarano and Poelma, 2009) and pitching airfoil (Buchner et al., 2012). TPIV employs multiple cameras (typically four) to simultaneously image seed particles from different viewing angles in order to reconstruct 3D Mie scattering fields. From these, the 3D velocity field can be determined through cross-correlation of subsequent particle fields. Recent studies have extended the use of TPIV to reacting flows (Coriton et al., 2014; Steinberg et al., 2015; Weinkauff et al., 2013; Tokare et al., 2014; Boxx et al., 2014).

The use of TPIV for combustion presents additional challenges, such as variations in particle seeding densities with gas density, increased imaging noise, and the potential of beam steering through index of refraction gradients. Furthermore, multi-kHz repetition-rate measurements mandate the use of either DPSS lasers having relatively low pulse energy, or rather complex pulse-burst laser systems (Roy et al., 2014). Nevertheless, the previous studies have demonstrated that high quality TPIV measurements can be made at repetition-rates exceeding 10 kHz using DPSS lasers in both non-premixed and premixed flames, albeit with a limited measurement volume.

Simultaneous velocity/scalar measurements often are made by combining PIV with PLIF of intermediate species of combustion (Peterson et al., 2013; Frank et al., 1999; Filatyev et al., 1998; Steinberg et al., 2011; Coriton et al., 2014; Petersson et al., 2007; Shimura et al., 2010). OH is a commonly targeted species for PLIF studies due to its high signal per unit laser fluence. OH is rapidly produced in the later stages of fuel oxidation and exists well into the hot combustion products. The transition from low to high OH therefore can be used as a marker of the onset of exothermic reactions, which spatially coincide with OH production (Leipertz et al., 2010).

Additional scalar information can be gained from the CH_2O molecule, which is formed during the initial stages of fuel breakdown and then rapidly consumed during exothermic reactions (Richter et al., 2005; Böckle et al., 2000; Temme et al., 2015; Ayoola et al., 2006). Furthermore, the product of OH and CH_2O concentration is related to the heat release rate, due to the role of these species in forming the HCO radical (Ayoola et al., 2006; Paul and Najm, 1998). CH_2O presents challenges in terms of excitation and detection. While several excitation schemes exist for CH_2O PLIF (Dieke and Kistiakowsky, 1934; Clouthier and Ramsay, 1983; Brand, 1956), among the most common is to utilize the high-energy, third-harmonic output of a Nd:YAG laser to excite the relatively weak sideband of the 4_0^1 transition around 355 nm. However, this transition results in relatively low fluorescence signal per unit laser fluence, which is particularly challenging for low pulse-energy DPSS lasers; multi-kHz repetition-rate CH_2O PLIF has predominantly been achieved using pulse-burst or laser-cluster systems (Gabet et al., 2012; Olofsson et al., 2006). The problem of low signal is further complicated if CH_2O PLIF is to be combined with PIV, as the excitation wavelength also can induce fluorescence of the solid seed particles used as flow tracers. Hence, low laser fluence results in low signal, while high laser fluence results in high noise from particle fluorescence. To the authors knowledge, the only previous application of simultaneous CH_2O PLIF and PIV was by Kuhl et al. (2013) to study the effects of electric fields on the motion of a laminar flame.

However, the knowledge gained by simultaneous time-resolved TPIV/OH PLIF/CH_2O PLIF measurements has the potential to provide considerable new insight into the behavior of turbulent flames. For example, Li et al. (2010) recently demonstrated considerable deviations in the scalar structure of turbulent premixed flames in the thin reaction zones and distributed reactions regimes from that of a laminar flame, including significant broadening of the CH_2O layer. Zhou et al. (2014) demonstrated potential broadening of the region containing exothermic reactions at even higher turbulence intensities, as measured by HCO PLIF. Temme et al. (2015) also showed considerable CH_2O broadening for flames in similar regimes. However, the overlap of the OH and CH_2O layers remained relatively thin. Understanding how these different flame structures are generated by the turbulence, the effect of the flame structure on reaction rate, and the effects of the flame on the turbulence are important for generating accurate and reliable models. Such information can be gained using time resolved vector/scalar measurements.

The remainder of this paper is organized as follows. First, the experimental configuration and diagnostics are presented, including a critical evaluation of the capability of the measurement techniques. Flame structures

elucidated from the simultaneous PLIF measurements are then discussed, including a method of extracting the 3D flame topology from the Mie scattering. Finally, a method of tracking fluid properties through space and time based on theoretical Lagrangian particles is discussed and various aspects of flame dynamics that can be quantified using this analysis are demonstrated. These include the dynamics of flame-flame interactions, measurements of the fluid residence time within the CH$_2$O layer, and the evolution of turbulence through the flame.
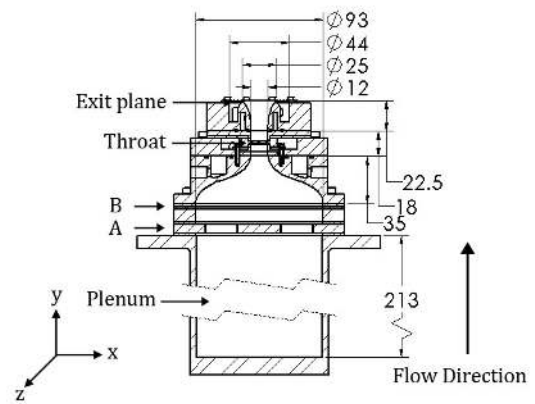
2 Experimental Configuration

The experiments were performed at the Air Force Research Laboratory, Wright-Patterson Air Force Base, and consisted of simultaneous 10 kHz TPIV, OH PLIF, and CH$_2$O PLIF (see Figure 1a) applied in a piloted premixed jet burner (called the Hi-Pilot burner (Skiba et al., 2015; Temme et al., 2015), Figure 1b). The setup included three high-repetition rate laser systems and six high-speed CMOS cameras, of which two cameras were equipped with intensifiers for the PLIF measurements. The Hi-Pilot burner consisted of a plenum, which fed the seeded premixed methane and air main flow through turbulence generating plates, to the nozzle. The turbulence plates are listed as A and B in Figure 1b, and their geometry is shown in Figure 21 in the Appendix. The coordinate system used is shown in Figure 1, with the origin of the coordinates at the center of the jet exit plane. An unseeded nonpremixed hydrogen pilot flame at the burner exit helped stabilize the flame. The geometry of the pilot exit plate is shown in Figure 22 in the Appendix.

Measurements were performed in three methane/air premixed jet flames at different bulk velocities ($U_{\rm J}$, ratio of volumetric flow rate to jet exit area, with exit diameter $D_e = 25$ mm) but at a constant equivalence ratio of $\phi = 0.85$ (see Table 1). Flow rates were controlled with calibrated electromechanical mass flow controllers, having an accuracy of approximately $\pm 1\%$ at the values used. One non-reacting case also was included, corresponding to the flow rates of Case 2 but without the pilot flow. Previous authors have reported sporadic detachment of the boundary layer near the burner exit resulting in intermittent side-to-side shifting of the flame brush using the Hi-Pilot burner (Temme et al., 2015), which necessitated the addition of an insert to reduce the nozzle divergence. This insert was not used in the present study as this phenomenon was not observed, likely as a result of the lower flow rates used.

To characterize turbulence at the burner jet exit and measurement locations, hot wire anemometry was
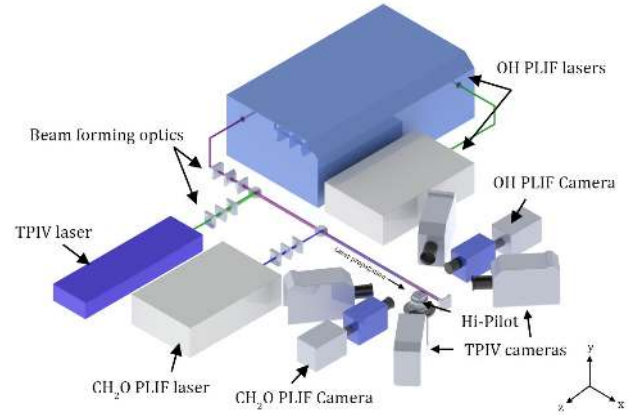
(a) Diagnostics configuration

(b) Hi-Pilot burner

Fig. 1 a Experimental configuration **b** Hi-Pilot geometry (dimensions in mm)

used at each flow rate, but without the flame lit and excluding the pilot. The hot wire was a single tungsten wire (5 μm diameter, 1.5 mm length), and the signal was recorded by a Dantec 56C01 CTA at a rate of approximately 32 kHz. Mean velocity ($\bar{u}_y$) and root-mean-squared velocity fluctuations (u'_y) at the exit plane are provided in Figure 23 in the Appendix; further details regarding exit plane turbulence are available from the authors.

For each of the three cases, measurements were performed at a variety of downstream locations, a subset of which exhibiting interesting phenomena are discussed here. The characteristic turbulence properties at the centerline of the jet exit ($\mathbf{x} = (0,0,0)$) and at the center of the laser measurement window ($\mathbf{x} = (0,y_m,0)$) for non-reacting flows corresponding to each case are provided in Table 1.

The turbulence Reynolds number was calculated as $\text{Re}_{\rm T} = u'_y \Lambda / \nu_r$, where Λ is the integral length scale, and ν_r is the kinematic viscosity of the reactants. The integral length scale was calculated from the local ve-

Table 1 Turbulence properties for each case based on hot wire anemometry, where U_{jet} is the bulk velocity, U_{cl} is the centerline velocity at the measurement location, and $\dot{m}_p$ is the mass flow rate of the pilot.

Case	U_{jet} (m/s)	$\dot{m}_p$ (g/s)	U_{cl} (m/s)	ϕ	y_m (cm)	y_m/D_t	Location	u'_y (m/s)	Re_T	$\lambda_k(\mu m)$	Ka	Da
1	1.9	0.008	6.8	0.85	2.0	1.6	Exit	0.40	87	236	5.0	40
							y_m	1.34	269	93	32.2	11
2	7.1	0.008	23.6	0.85	4.0	2.56	Exit	2.19	464	99	28.5	16
							y_m	5.50	2092	39	188.6	5.2
3	11.1	0.015	25.7	0.85	4.0	3.2	Exit	4.21	2794	54	97.9	12
							y_m	10.16	5738	27	396.8	4.1

locity autocorrelation using the hot wire measurements, and invoking Taylor's hypothesis of frozen turbulence. The Kolmogorov microscale was then calculated as $\lambda_k \approx 2\Lambda Re_T^{-3/4}$. Karlovitz and Damköhler numbers were respectively calculated as $\text{Ka} = \left(\lambda_k/\delta_l^0\right)^2$ and $\text{Da} = (S_L^{0\,2}/\nu_r)/(u'_y/\Lambda)$, where a Schmidt number of unity is assumed. The flame thermal thickness (δ_l^0) and the laminar flame speed (S_L^0) were calculated from a 1D laminar flame simulation in Cantera using the GRIMech 3.0 chemical mechanism as $\delta_l^0 = 0.53$ mm and $S_L^0 = 27$ cm/s (Goodwin, 2003).

The conditions at each measurement location and the jet exit for the three cases are shown in the regime diagram of Williams (1976) in Figure 2. Red circles with subscript t represent the test locations, and green circles with subscript e represent the jet exit. Note that the turbulence intensity increases at the measurement locations relative to the jet exit due to shear with the quiescent surrounding air.
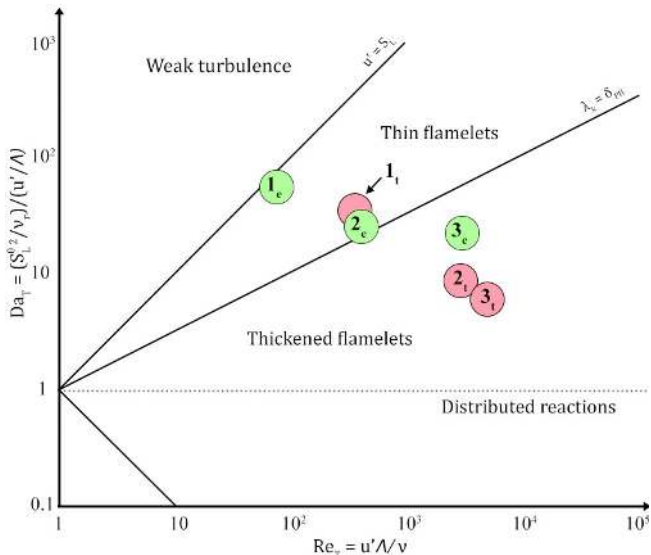
Fig. 2 Conditions for Cases 1-3 at both the test location and the burner exit plane (subscripts t and e respectively) on the regime diagram of Williams (1976).

2.1 Tomographic Particle Image Velocimetry

A diode pumped solid state Nd:YAG laser (Quantronix Hawk-Duo 532-120-M) and four high-speed CMOS cameras (Photron SA-Z) was used for the TPIV setup. The laser had two independently controlled heads, each providing 6 mJ/pulse at a repetition-rate of 10 kHz. After beam expansion and collimation, two knife edges were used to clip the laser, forming a rectangular volume. The volume width was measured to be 2.5 mm by traversing a thin slit through the beam profile, where the edges were defined to be at 25% of maximum measured power. After volume forming, the pulse energy at the measurement location was 2.9 mJ/pulse. A delay of between 3-15 μs was used between the TPIV laser pulses, depending on the case, to allow sufficient inter-frame particle displacement for accurate velocity calculations.

The seed particles were titanium dioxide having a mean diameter of approximately 1 μm, which corresponded to Stokes numbers between 0.01-0.03 for the different cases. The characteristic flow time used in the Stokes number calculation is taken relative to the eddy turn-over time of the smallest resolved spatial scales (σ, described further below) as $\tau_\sigma = \sigma^{2/3}\Lambda^{1/3}/u'_y$. Laser light scattering from the particles was simultaneously imaged onto the four CMOS cameras, each operating at 20 kHz in a frame-straddling mode. The cameras used the full sensor at this repetition rate (1024×1024 pixels). Two cameras were mounted in forward scatter and two in backwards scatter configuration, respectively oriented at angles of approximately 40° and 30° to the laser sheet normal direction. A 180 mm imaging objective (Tamron Telephoto, focal length= 180 mm, f/# = 8) was equipped on each camera, and tilted relative to the detector using a Scheimpflug adapter to prevent off-axis image blurring. It was found during the experiment that the similar aperture settings were able to achieve comparable signals despite the higher efficiency of the forward scatter configuration. Furthermore, the lens configuration provided sufficient depth of field to maintain good focus across the laser volume. The final reconstructed volume was approximately 25×15×2.5 mm³ after post-process clipping of the field-of-view (FOV).

Camera calibration and registration was performed by using a custom thin-film transparent dot target. Dots

with diameters of 0.538 mm and spacing of 3.705 mm were printed on one side of a transparency with a thickness of approximately 0.15 mm. Target images were recorded on the four TPIV cameras at seven equally spaced z-planes (0.6 mm between planes), with the z = 0.0 mm plane coinciding with the OH and CH$_2$O PLIF laser sheets.

Velocity vector calculation was performed using commercial software (DaVis 8.2.2, LaVision) and consisted of camera volume calibration, preprocessing of the particle images, camera self-calibration, reconstruction of the 3D particle field, determination of the local velocity vectors, and post-processing of the vector fields. The target images were used for the initial camera calibration. Raw particle image preprocessing was then performed to remove background noise and better identify particles. A volume self-calibration was then performed using the preprocessed particles in order to further refine the camera calibration until the triangulation error was sub-pixel (typically around 0.5 pixels). The 3D particle field was then reconstructed using seven iterations of the multiplicative algebraic reconstruction tomography (MART) algorithm. The size of the reconstructed volume varied slightly between data sets, but was approximately $25{\times}15{\times}2.5$ mm^3, which corresponds to $962{\times}577{\times}96$ voxels (vx). Inter-frame particle displacements were determined by performing a multi-pass direct volume correlation at a final window size of $24{\times}24{\times}24$ vx with a 75% overlap, resulting in a 632 μm interrogation box size and a 156 μm vector spacing. Finally, a universal outlier detection, removal, and insertion algorithm was used to reduce spurious vectors. Ghosting levels were calculated by examining the z-profile intensity as recommended by the software manufacturers. Ghost levels were calculated as 10 - 35% between the four cases.

Figure 3 shows an example of a reconstructed particle field and corresponding velocity vector field. In Figure 3a, there are two distinct levels of particle number density, which correspond to the decrease in gas density between the reactants and products. During the experiment, seed particle density was adjusted in an attempt to achieve a good balance between the reactants and products. Higher seeding densities, which provided better seeding in the products, created problems in reactant particle field reconstruction due to a high level of particle image overlap. More seed also resulted in increased noise in the PLIF images, which was particularly challenging for the CH$_2$O PLIF. As the flow upstream of the flame is the most important for flame structure and dynamics, the seed density therefore was primarily optimized for good vector calculation in the reactants. The resultant seeding density in the reactants was around 0.05 particles per pixel, as recommended in
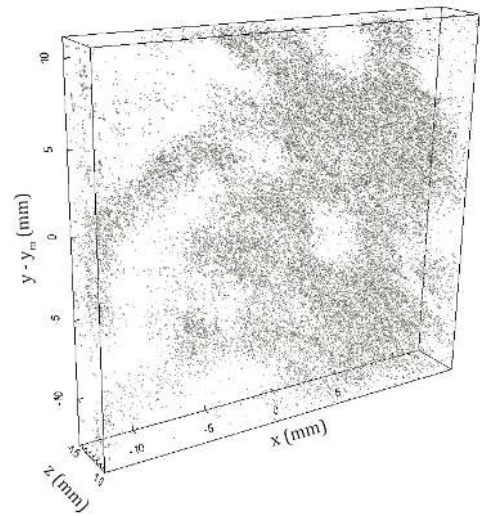
(a) Reconstructed 3D Particle Field
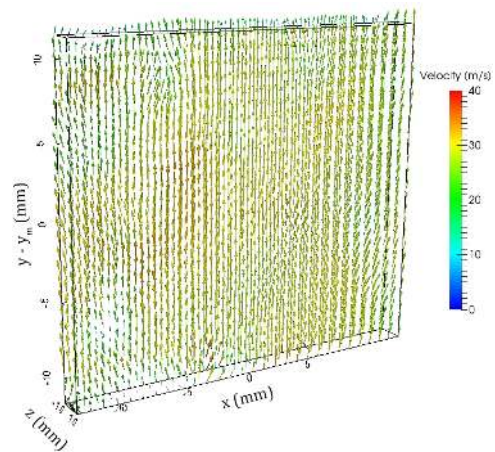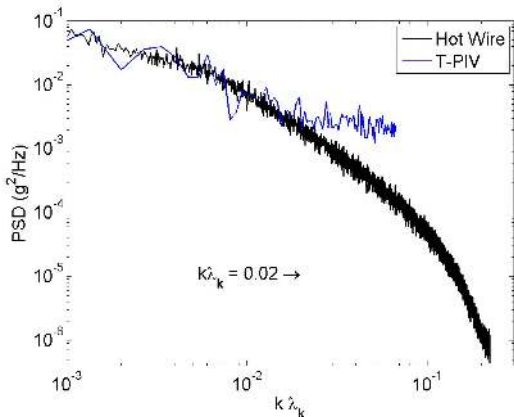

(b) 3D Vector Field

Fig. 3 Typical TPIV results from Case 2. **a** Reconstructed instantaneous particle field. **b** Corresponding velocity vectors (one in 6^3 vectors shown for clarity)

Elsinga et al. (2006), corresponding to approximately 30 particles/mm^3.

2.1.1 Assessment of Velocity Measurements

TPIV in flames is a relatively new diagnostic, and assessment of the resultant velocities therefore is necessary. As PIV measurements are based on the displacement of multiple particles within a finite sized interrogation volume, there is an inherent averaging of calculated velocity vectors. Moreover, removing noise artifacts via post-processing smoothing can remove small-scale turbulence. In order to examine the effective TPIV resolution, the 1D turbulent energy spectrum determined via the hot wire measurements was compared to that determined via TPIV in a non-reacting jet with flow

conditions matching Case 2, as shown in Figure 4. The point where the two energy spectra diverge was around $k\lambda_k = 0.02$, which for Case 2 corresponds to $\sigma \approx 1.9$ mm, or about 3 times the interrogation volume size. Note that the hot wire spectrum was calculated from the temporal signal by invoking Taylor's hypothesis, whereas the TPIV spectrum was calculated from the spatial fluctuations at each measurement instant.

Table 2 Spatial and temporal resolution parameters

Case	FOV mm (pix)	σ mm	$\tau(\sigma)$ ms	C_e	D_e	D_e/C_e
1	26×17 (1026×654)	1.93	1.68	0.06	1.3	22.0
2	27×20 (1044×780)	1.93	0.52	0.19	1.6	8.4
3	27×24 (1044×942)	1.93	0.31	0.32	2.1	6.7

Fig. 4 1D turbulent energy spectra for non-reacting Case 2 from hot wire and TPIV

Fully resolving the vorticity and strain tensors is possible with the 3D/3C velocity vector measurements of TPIV, subject to the resolution limitations of the diagnostics. In practice however, these values are particularly susceptible to noise artifacts, as they are based on velocity gradients. Smoothing the velocity field will reduce the noise in the velocity gradient measurements, but also reduce the measured magnitude of true gradients. To examine this, the enstrophy field was compared to the divergence field in non-reacting flow with different amounts of smoothing as in Coriton et al. (2014). Conservation of mass in constant density flows requires that $\nabla \cdot \mathbf{u} = 0$, and deviations from this condition represent noise in the velocity gradient calculations. Three smoothing schemes were examined, a moving average (i.e. box), Gaussian, and penalized least squares filter kernel (Garcia, 2010) with various smoothing parameters. All smoothing schemes followed similar trends, and only the results from the penalized least squares method with a smoothing parameter of $s = 0.5$ are discussed here.

Figure 5 shows a joint PDF of smoothed and unsmoothed enstrophy. While the smoothing reduced the calculated enstrophy, the smoothed and unsmoothed values remain highly correlated. This indicates that the measured enstrophy structures are spatially coherent. Conversely, the joint PDF of smoothed versus un-

smoothed divergence shows essentially no correlation, as demonstrated in Figure 5b. This implies that smoothing maintains the structure of the enstrophy field while reducing the noise levels. The penalized least squared method with $s = 0.5$ was found to provide a good balance of preserving the enstrophy and reducing the divergence, and hence was used for all subsequent analysis.

Furthermore, the relation between noise and true velocity gradients was examined by plotting a joint PDF of enstrophy and squared divergence, given in Figure 5c. As shown, large values of divergence correspond to small enstrophy values, and vice versa, indicating that large velocity gradients tend to be more accurately measured than small gradients. This observation has been reported numerous times for TPIV measurements (Coriton et al., 2014; Scarano and Poelma, 2009; Worth et al., 2010; Baum et al., 2013).

Finally, the adequacy of the temporal resolution and TPIV measurement domain to capture the dynamics of the turbulence was investigated. These can be respectively quantified by $C_e = \Delta t_m/\tau(\sigma) \leq \frac{1}{2}$ and $D_e = \tau_{res}/\tau(\sigma) \geq 1$ (Coriton et al., 2014; Steinberg et al., 2015), where Δt_m is the measurement temporal resolution, τ_{res} is the residence time of flow structures in the measurement domain (i.e. $\tau_{res} = L_{fov}/\bar{u}_y$, where L_{fov} is the length of the TPIV volume in the y-direction). The ratio of these parameters (i.e. $D_e(\sigma)/C_e(\sigma) = \tau_{res}/\Delta t_m$) indicates how well the large-scale flow dynamics are resolved; larger values correspond to measurements for which the large-scale flow dynamics are captured. As shown in Table 2, the temporal criteria were satisfied in all cases, indicating that the dynamics of the smallest resolved spatial scales are fully resolved in time and captured in the FOV.

2.2 Planar Laser Induced Fluorescence

The scalar measurements consisted of simultaneous OH and CH_2O PLIF. The OH PLIF system used the second harmonic output of a Nd:YAG laser (EdgeWave Innoslab HD40II-ET, 532 nm, 10 mJ/pulse) operating at 10 kHz to pump a dye laser (Sirah Credo) with Rhodamine 6G dye solution, and a high-speed CMOS camera (Photron SA-5) coupled to an image intensifier (LaVision IRO,

(a) Enstrophy   (b) Divergence   (c) Enstrophy vs. Divergence
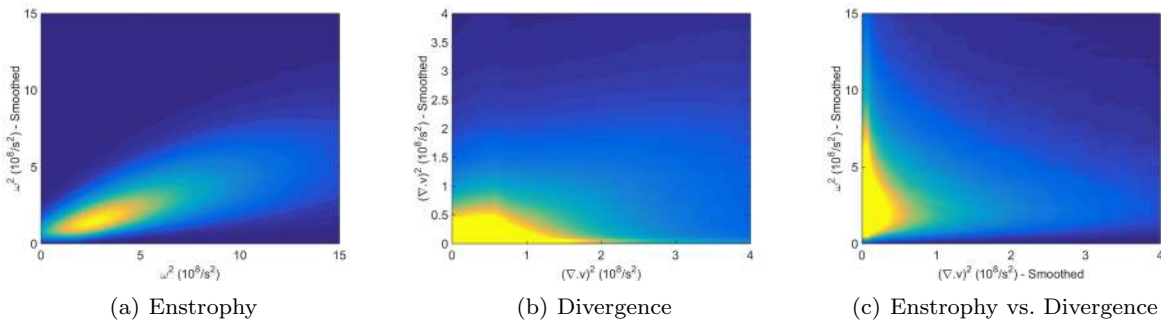
Fig. 5 Effects of smoothing on velocity gradients. **a** Smoothed and unsmoothed enstrophy. **b** Smoothed and unsmoothed divergence. **c** Smoothed enstrophy and divergence. All smoothing is performed using a penalized least squares method with $s = 0.5$.

gate = 200 ns). The frequency doubled dye laser output (0.2 mJ/pulse) was tuned to excite the Q$_1$(7) line of the A-X ($v' = 1$, v''=0) band of OH at approximately 283.2 nm. The formed laser sheet had a height of approximately 30 mm and a thickness of approximately 0.3 mm at the measurement location, determined in the same manner as for the TPIV volume. The pixel size was ca. 26 μm, although the effective spatial resolution of the images is limited by the sheet thickness. Fluorescence in the range of 310 nm was isolated using a bandpass filter, and collected into the intensified camera using a fast UV lens (Sodern Cerco, focal length = 100 mm, f/# = 2.8). At 10 kHz, the camera had an active imaging array of 896 × 848 pixels.

The CH$_2$O-PLIF setup consisted of a frequency tripled Nd:YAG laser (EdgeWave Innoslab IS12II-E, 355 nm, 2.8 mJ/pulse) operating at 10 kHz, and the same lens, intensifier, and camera system as for the OH PLIF system. However, the intensifier gate time was reduced to 100 ns to reduce background flame emissions. The pulse energy of the 355 nm laser at the measurement location after sheet formation was 1.6 mJ. A concave cylindrical mirror, coated for 280-355 nm, is used to retro-reflect both the OH and the CH$_2$O beams back through the probe volume, which effectively doubled the PLIF signals.

The laser excited the A-X4$_0^1$ transition of formaldehyde in a bandwidth around 355 nm. To better concentrate pulse energy, the sheet height was set smaller than the TPIV and OH PLIF beams at 7.5 mm. Fluorescence in the range of 370-480 nm was isolated using a Schott KV-389 filter.

The two PLIF pulses were separated by approximately 700 ns, and occurred between the TPIV pulses for each measurement. The position of the PLIF sheets concided with the center of the TPIV beam. A 3rd order polynomial warping algorithm was used to match the target images of the PLIF and TPIV, where the PLIF

target image was the thin-film transparency on the z = 0.0 mm plane.

The low fluorescence yield of the CH$_2$O and low pulse energy requires careful evaluation of the signal-to-noise ratio (SNR) and the conclusions that can be drawn from the measurements. Particular care was taken here to ensure that interpretation of the data was robust to the SNR and any image processing performed to aid in visualization. Typical recorded PLIF images from Case 3 (lowest SNR) are shown in Figure 6a, where red represents the OH PLIF and blue is the CH$_2$O PLIF. As seen qualitatively, there is substantially more noise in the CH$_2$O PLIF images than in the OH images. Despite this, there are discernible structures present in the CH$_2$O fields; there are regions of low CH$_2$O in the products (OH containing regions) where the CH$_2$O has been consumed and in the fresh reactants prior to OH formation.

Processing of the raw CH$_2$O images included applying a 4×4 bin, subtracting a calculated noise level, applying a 5×5 median filter to remove noise 'speckles', and finally applying a 3×3 Gaussian filter to further smooth the images. Identifying the CH$_2$O-containing regions was then done by thresholding the images. To ensure the data presented was independent of the image processing, this thresholding parameter was varied between 50% and 200% of the final value used in all data sets. No difference was found in the location of the identified CH$_2$O-containing regions across this range of thresholds. Hence, the qualitative identification of CH$_2$O containing regions was robust despite the relatively low SNR.

The SNR was quantified as the mean signal in the the regions containing CH$_2$O (as defined above) to the mean signal in regions not containing CH$_2$O. The SNR was calculated based on the raw images (not the processed images) and found to range from 2.6-5.6 for the different cases. As will be discussed below, the CH$_2$O-containing region became broader with increasing turbulence inten-

sity, resulting in lower concentrations and lower SNR with increasing turbulence.

Donbar et al. (1997) reported the contribution of seeding particles to background noise in CH PLIF measurements, which was also observed here in the CH_2O measurement; increasing the seed flow increased the background noise. Images therefore also were taken with no seed to ensure that all interpretation was robust. The data without seed typically had a SNR approximately 20-50% higher than data with seed, and no qualitative change was observed in flame structure as a result of this higher SNR. It is noted that TPIV is somewhat advantageous in this respect, as it requires lower seed number density than planar PIV.

Despite the high SNR of the OH, processing of the OH images was done to remove horizontal striations caused by laser sheet inhomogeneity, which are visible in Figure 6a. These were found to be transient in time, and thus unable to be removed with a time-averaged sheet-correction. Instead, a shot-to-shot correction was applied based on the instantaneous images. To do so, an instantaneous image was first thresholded into regions with and without OH. The total OH signal in each row from the original image was then normalized by the number of pixels containing OH in that row, resulting in a conditional mean OH value for that row. Finally, each row of the original image was normalized by its conditional mean, producing a relatively smooth OH field for the purposes of image processing.

Figure 6b shows processed OH and CH_2O images for Case 3. It is noted that such images are not intended to be viewed quantitatively, and the included color scale is for reference purposes only. From these images, it is clear that the measurements can robustly separate the CH_2O containing regions from those without CH_2O in the products (regions with OH) and in the fresh reactants.

3 Results

3.1 Flame Structure

Before discussing the turbulence and flame dynamics, it is necessary to understand the flame scalar structure and topology at the different conditions studied. This can be achieved using the simultaneous PLIF measurements, in combination with the 3D Mie scattering fields associated with the TPIV.

Sample images showing the superposition of the OH and CH_2O PLIF for Cases 1-3 are shown in Figure 7. Figure 7a shows a very clear laminar-like structure to the CH_2O layer at the low turbulence intensities of Case 1. The transition from low-to-high OH signal is

sharp and the OH and CH_2O do not broadly overlap, indicating thin heat release regions. This is consistent with the flame being in the laminar flamelet regime.

The images in Figure 7b of Case 2 shows examples of CH_2O layer merging, the formation of detached reactant pockets through flame-flame interaction, as well as examples of both flamelet-like and broadened CH_2O regions. Similar to Case 1, the OH gradients are sharp and the overlap between OH and CH_2O is thin. Hence, Case 2 appears to be a transitional state between the laminar flamelet and thickened preheat zone/thin reaction zones regimes.

As the turbulence intensity increases to Case 3 in Figure 7c, CH_2O appears more broadly distributed. There is little correlation between the topology of the OH layer and the upstream (reactant side) of the CH_2O region, which has numerous turbulence-induced structures, e.g. long CH_2O 'fingers' protruding into the reactants. However, Case 3 continues to show sharp OH transitions and low overlap between CH_2O and OH. While there is significant local extinction in both cases as indicated by the discontinuities in the OH layer, there is no evidence of broadly distributed heat release. This flame therefore is characterized by broadened preheat zones and thin (but broken) reaction zones. Quantification of the flame thickness will be discussed in Section 3.2.3.

When investigating flame structure and topology from 2D measurements, it is important to account for the 3D nature of the flame. For example, significant out-of-plane orientation can result in perceived thickening of scalar layers in planar images. Three dimensional measurements of flame structure have been made by tomography (Xu et al., 2015; Floyd et al., 2010; Moeck et al., 2013), multi-plane measurements (Trunk et al., 2013), and scanning mirror measurements (Wellander et al., 2014). However, each of these has some drawbacks for the current application. Tomography requires several simultaneous views to reconstruct the 3D field from 2D projections. High resolution requires a large number of views, which was not optically viable in this experiment. Furthermore, accurate reconstruction requires quantitative scalar signals from each of the views, which is difficult to achieve due to e.g. quenching and signal self-absorption. Multi-plane measurements also require additional detectors and lasers, which was not possible. Furthermore, such measurements provide limited 3D resolution, generally utilizing only two planes for practical reasons. The limitation in number of planes is alleviated in scanning mirror measurements, but the data are no longer instantaneous. Extremely high scanning and measurement rates would be required to effectively freeze the flows studied here, which was not experimentally viable.

(a)

(b)
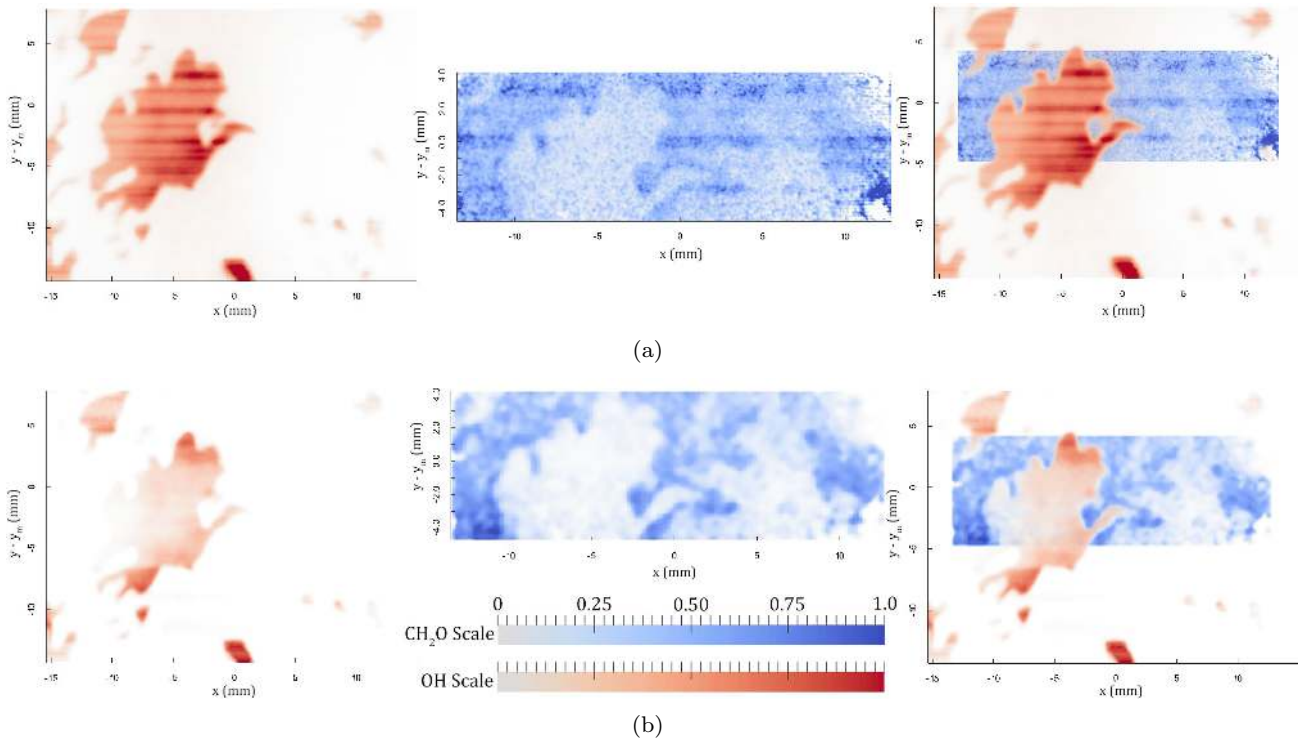
Fig. 6 Example of OH PLIF (red), CH₂O PLIF (blue), and overlap from Case 3. **a** Typical raw images. **b** Processed images.

Instead, the Mie scattering tomography was used to gain insight into the 3D flame geometry. Mapping the 2D topology of turbulent premixed flames in the laminar flamelet regime using Mie scattering previously has been done by utilizing the drop in particle number density between reactants and products (Steinberg et al., 2008; Stella et al., 2001). For seed that does not survive the flame, such as olive oil, the density drop is sharp near a particular isotherm where the seed evaporates. For solid particles that survive the flame, such as the titanium dioxide used here, the decrease in particle seed density is a result of the decrease in gas density as the reactants expand to the products.

Here, this technique is extended to 3D by utilizing the Mie scattering volumes that are tomographically reconstructed as part of the TPIV processing. The particular challenge for tomography is that the volumetric number density of seed particles is lower than for planar PIV applications, so as to avoid excessive seed particle overlap in the different viewing angles. This has the potential to add noise and reduce resolution in the topology measurements. Nevertheless, a sharp decrease in seed particle density was observed in most cases, as was shown in Figure 3a for Case 2.

To reconstruct the corresponding 3D topology, the overall volume first was binned into 10×10×10 voxel subvolumes. A Gaussian filter was then applied with a window size of 5 subvolumes, and a standard deviation

of half the window size. The images were then thresholded to delineate products and reactants, and a hole fill algorithm was applied; the choice of threshold value is discussed below. The 3D flame surface thus determined from the Mie scattering field in Figure 3a is shown in Figure 8.

Properly selecting the threshold value is critical for accurately defining the 3D flame topology. While the topology of laminar flamelets (e.g. Case 1) is relatively simple to define since density gradients are sharp and scalar isosurfaces are parallel, the distributed CH₂O regions observed in Cases 2 and 3 indicate reduced density gradients and non-parallel isosurfaces. However, the observation that OH gradients remain sharp and CH₂O/OH overlap regions remain thin for all cases indicates that it may be possible to extract a topological surface from the Mie scattering that corresponds to the generation of OH. Such a surface would represent the reactant side of the thin heat release layers.

To determine the optimal threshold value for identifying this surface, 3D flame topologies on the $z = 0$ plane were compared to OH PLIF images at various threshold levels. The OH images were binned to match the resolution of the 3D flame, binarized to distinguish product from reactants, and then compared to the 3D reconstruction. To make the comparison between the OH and reconstructed flame, the 2D projection of the 3D flame topology and the curve repre-

(a) Case 1

(b) Case 2

(c) Case 3
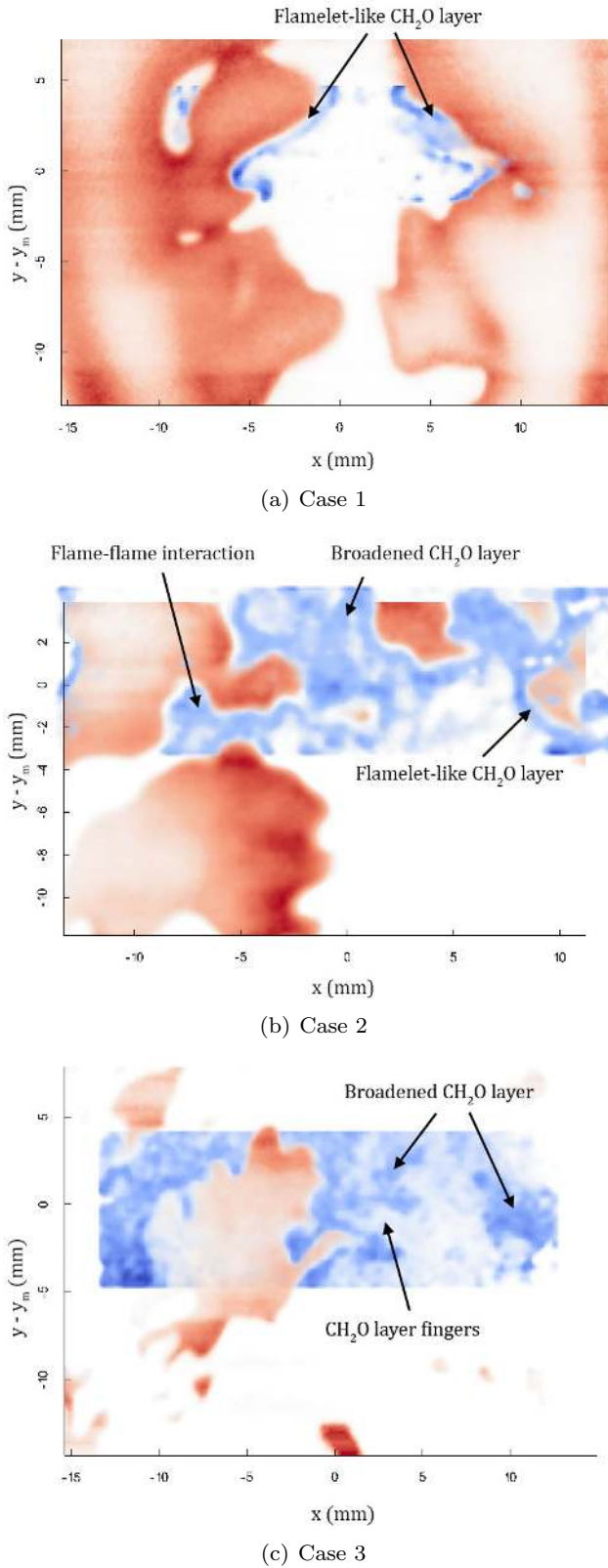
Fig. 7 Typical OH PLIF and CH_2O PLIF images for Cases 1-3. Color scale as per Figure 6
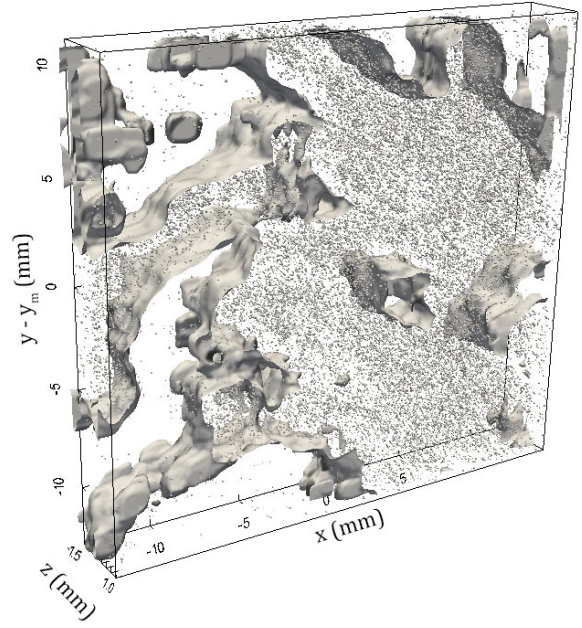

Fig. 8 Reconstructed 3D flame corresponding to the Mie scattering field in Figure 3a

senting the OH were each represented as parametric space curves, $\zeta_{3D}(\xi_{3D}) = x_{f,3D}(\xi_{3D})\hat{i} + y_{f,3D}(\xi_{3D})\hat{j}$ and $\zeta_{OH}(\xi_{OH}) = x_{f,OH}(\xi_{OH})\hat{i} + y_{f,OH}(\xi_{OH})\hat{j}$. As ξ_i increases, $x_{f,i}$ and $y_{f,i}$ trace out the different flame curves. For each value of ξ_{3D}, the minimum distance between ζ_{3D} and ζ_{OH} was calculated. This process was repeated using various threshold levels for the 3D reconstructions, and the final 3D flame was chosen based on the minimum mean difference between the two curves across all images.

Using the final selected threshold value for the 3D reconstruction, statistics on minimum distance between ζ_{3D} and ζ_{OH} was determined, which are presented in Figure 9 for Cases 1-3. As the ability to reconstruct the 3D flame depends on both the flow density gradient across the flame and the seeding density, the accuracy of the reconstruction is highly case dependent. Case 3 had the lowest accuracy of the three reconstructions through a combination of relatively low seeding density and shallow density gradients.

Figure 10 shows an example cross-section of the 3D topology superimposed on the OH PLIF plane for Cases 1-3. As can be seen, the 3D topology is capable of capturing the general shapes and structure of most OH layers. However, because the 3D reconstruction is based on the distribution of particles, the reconstruction can deviate from the OH PLIF for two main reasons. Firstly, natural inhomogeneity in the seeding flow or laser illumination can result in local volumes of reactants with low seed. This tends to result in regions with rather smooth deviation between the OH and 3D flame, as seen to-
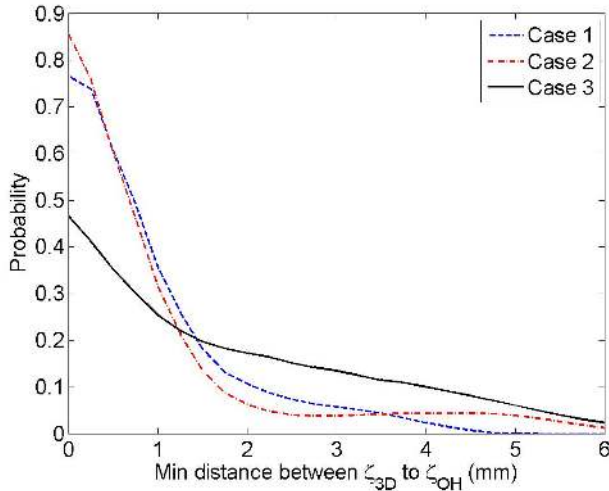
Fig. 9 Minimum distance between ζ_{3D} and ζ_{OH} for Cases 1-3

wards the bottom of Fig. 10a. Secondly, the binning and smoothing of the particle field reduces the effective spatial resolution of the measurements, resulting in the 3D reconstruction occasionally missing fine-scale features such as that around (-5 ,-3 mm) of Fig. 10a.

Despite these issues ,the 3D reconstructed can be used to deduce the general 3D flame shape and orientation. For example, Figure 8 suggests that flame orientations in the z-direction are uncommon for Case 2. To quantify this, 3D flame surface normals ($\hat{\mathbf{n}}$) were calculated from the Mie scattering surfaces for each case. The PDFs of the flame normal components are shown in Figure 11a for Case 3. Normals for Cases 1-2 are similar to Case 3, but are not presented here. As can be seen, there is a high propensity for $n_z = 0$, which indicates that the planar measurements capture the majority of the flame structure information. The low values of n_z likely are due to the jet flame configuration, which produces non-isotropic turbulence that predominantly wrinkles the flame surface in the $x - y$ plane. The increased probability of n_y towards -1 is because the flame is conically shaped and therefore preferentially points in the negative y direction. The increased probability of n_x and n_z towards -1 are because the FOV is off-centered along these two directions, and thus predominantly captures one half of the flame. Also included are the 2D flame normals (x and y components) computed directly from the OH PLIF in Figure 11b. This is overlay with the flame normal computed from a plane of the Mie scattering surface on the OH PLIF plane as a direct comparison, which shows good agreement between the two.
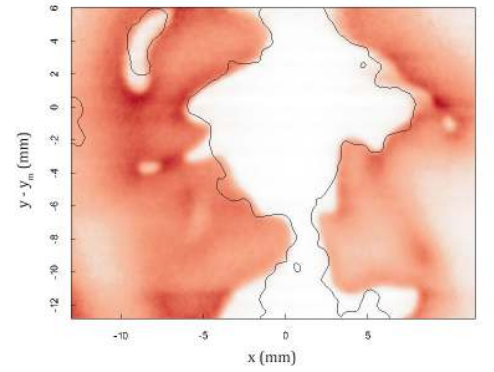

(a) Case 1
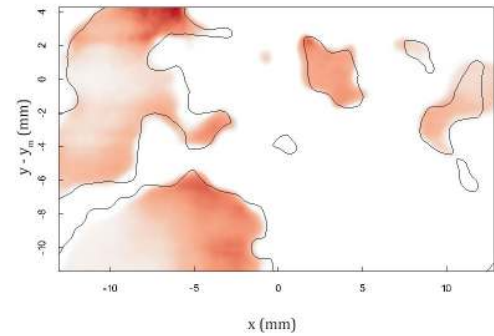
(b) Case 2
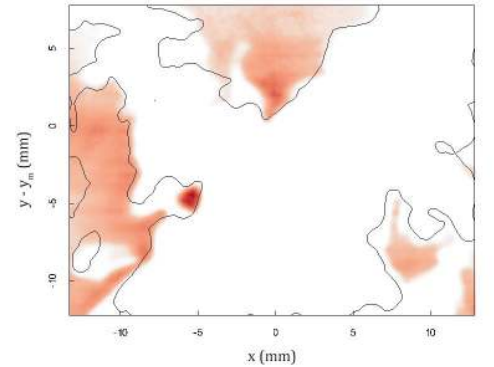
(c) Case 3

Fig. 10 Typical 3D reconstructed flame at the z = 0 mm plane (solid line) with corresponding OH PLIF for Cases 1-3.

3.2 Flow and flame dynamics

3.2.1 Lagrangian particle dynamics

The availability of 3D time resolved velocity fields allows for the tracking of theoretical Lagrangian particles (TLP) through the flow field. TLPs are massless and non-diffusive 'particles' that are computationally placed in the measured velocity fields and move with the flow. The TLPs act as passive flow tracers, allowing calculation of various properties along Lagrangian trajectories

(a)

(b)
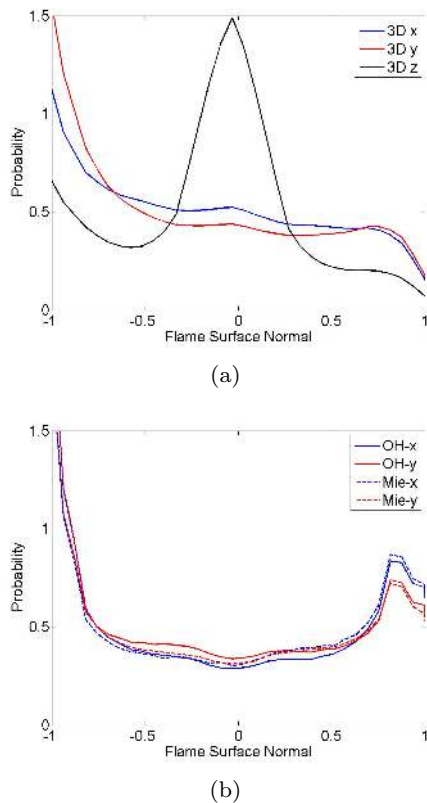
Fig. 11 Flame surface normals for Case 3. **a** 3D normals from Mie scattering surface. **b** 2D normals from OH contour and Mie scattering surface

as the particles interact with the flame scalar structure (Steinberg et al., 2015).

The use of TLPs to study the Lagrangian behavior of turbulence is well established for DNS data sets (Fukushima et al., 2014), but has not been widely employed for experimental measurements due to the lack of time-resolved 3D velocity fields. At a time t^*, the position of particle j having an initial position of $\mathbf{X}_{j,0}$ at time $t_{j,0}$ is $\mathbf{X}_j \mid_{t^*} = \mathbf{X}_j \left(\mathbf{X}_{j,0}, t_{j,0} \mid t^* \right)$. The evolution of the particle position is governed by

$$\frac{d\mathbf{X}_j}{dt} \bigg|_{t^*} = \mathbf{U}_j|_{t^*} \tag{1}$$

where $\mathbf{U}_j|_{t^*} = \mathbf{u} \left(\mathbf{X}_j \mid_{t^*}, t^* \right)$, $\mathbf{U}$ is the Lagrangian velocity and $\mathbf{u}$ is the Eulerian velocity. This formulation essentially treats the TLPs as passive, massless, non-diffusive flow tracers that follow the velocity field.

Accurately solving Eq. 1 is not trivial, particularly for finite resolution experimental data that exhibits noise. Here, the tracking scheme of Steinberg et al. (2015) is used, which employs four interpolated time steps between each measurement time. Cubic spline interpolation is used in both space and time, which has been shown to be sufficient to account for the non-linearity of

turbulence (Yeung and Pope, 1988). TLPs were placed into the measured velocity field with a density corresponding to the inter-vector spacing from the TPIV. As particles left the measurement volume, new particles were inserted in open locations, thereby keeping the total number of particles constant.

An issue that arises with TLP tracking through experimental data is that erroneous local instantaneous vectors can cause considerable error in the evolution of an individual particle; once error is induced in the particle position, this error grows exponentially with time. While erroneous vectors could be reduced through increased outlier detection or smoothing, these methods also affect the other non-erroneous vectors. It therefore was decided to track ensembles of particles together, instead of individual particles.

The idea is shown conceptually in Figure 12 for a 2D configuration. An ensemble of particles in the reactants convect in the flow direction. The centroid is taken as the characteristic position of the ensemble. Individual outlier particles caused by measurement noise can be identified based on the mean velocity in the ensemble, and eliminated from the centroid calculation. After each time step, a new ensemble of particles is identified around the centroid of the previous ensemble, and used for the subsequent time step. For all analysis here, the chosen ensemble size was selected to be equal to the interrogation volume size, and thus contained about 125 individual vectors in a ca. 0.6 mm sided cube due to the interrogation volume overlap.
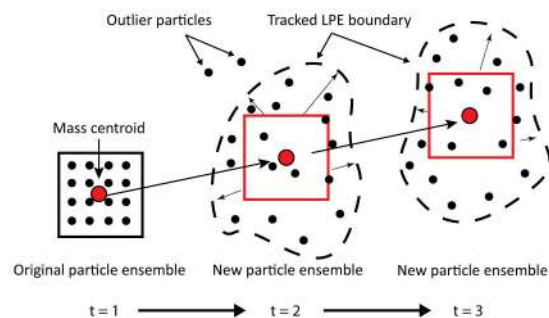
**Fig. 12** Concept of Lagrangian particle ensemble (LPE) tracking

Tracking errors are cumulative when calculated across multiple time steps. In order to quantify these errors, particle ensembles were tracked in a variety of test flow fields. The test flow fields were designed to produce similar cumulative errors in TLP tracking as would be anticipated in the experimental flows. To that end, the fields had a constant shear rate of $S = \partial u_x / \partial y$, superimposed on a uniform convective velocity ($\bar{u}_y$). Different

values of S were selected to represent different strengths of turbulence, and the convective velocity was set to be approximately that of Case 2. Hence, the velocity fields were given by $\mathbf{u} = (Sy, \bar{u}_y, 0)$. From this, the ideal position ($\boldsymbol{\chi}$) of a particle at some time t^*, that started at an initial position $\mathbf{X}_{j,0} = (x_0, y_0, 0)$ is

$$\boldsymbol{\chi}_j \mid_{t^*} = \left(\frac{S(\bar{u}_y t + y_0)^2}{2\bar{u}_y} + \left[x_0 - \frac{Sy_0^2}{2\bar{u}_y} \right], \bar{u}_y t + y_0, 0 \right) \tag{2}$$

The exact particle positions were compared to those calculated using the TLP ensemble tracking algorithm. The algorithm was applied to the test vector fields sampled at 150 μm vector spacing and 0.1 ms between tracking time steps, which was the same as the experiment. Moreover, to account for the effects of noise in the measurements, $\pm 0.05\bar{u}_y$ of normally distributed white noise was added to the test flow field.

An example of the exact and tracked particle positions is shown in Figure 13 for $S = 10^3$ s^{-1} over 6 time steps, after which a portion of the particle ensemble left the domain. To quantify the error over time, the difference between tracked and exact positions ($|\boldsymbol{\chi}_j \mid_{t^*} - \mathbf{X}_j \mid_{t^*}|$) were measured at each time step and each value of S. This tracking error was calculated over a range of S values, shown in Figure 14 as a function of tracking time. Tracking errors typically were less than about 1 mm, even for flow exposed to the highest velocity gradients for long durations. This tracking algorithm will be applied in the following sections.
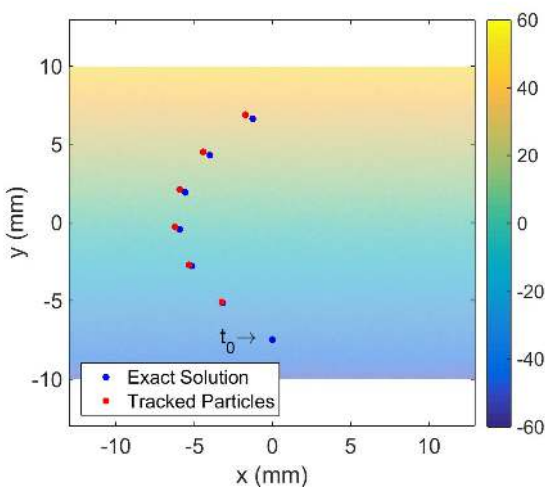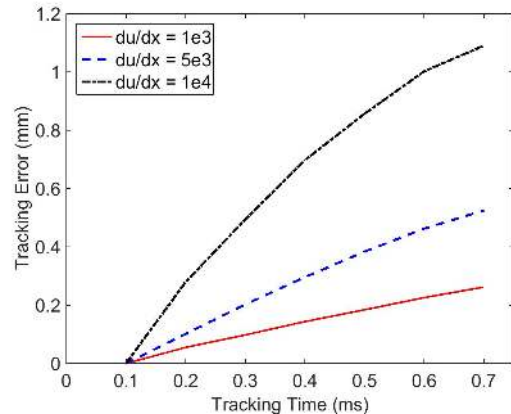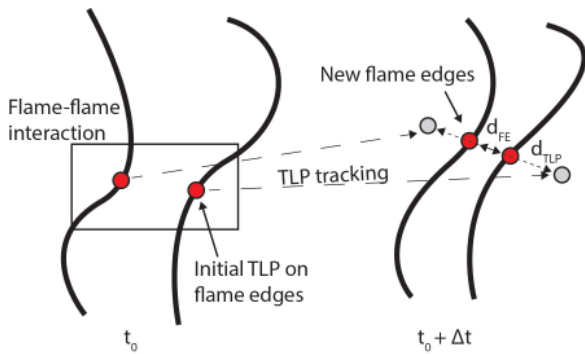

Fig. 14 Error in particle tracking as a function of number of time steps

3.2.2 Flame-Flame Interactions

Turbulent combustion can lead to flame structures that propagate towards one another. These regions can be due to negative curvature (concave towards the reactants), thin 'necks' due to propagation of roughly parallel flames, or pockets of reactants burning in the products. In the former case, negative curvature corrugations may be induced by the turbulence or flame instabilities, which may grow into long reactant 'fingers' protruding into the products due to pressure gradients across the flame surface (Poludnenko and Oran, 2010, 2011; Lipatnikov et al., 2015; Buschmann et al., 1996; Shepherd and Cheng, 2001; Chen and Bilger, 2002, 2004; Steinberg et al., 2008; Wang et al., 2013).

Flame-flame interactions result in destruction of flame surfaces via merging, and hence a reduction in the local reaction rate. This merging has been shown to be mainly due to edge flame propagation and not as a result of the turbulence-induced convection (Lipatnikov et al., 2015). However, increased local reaction rates also have been observed in regions of flame-flame interaction, which can increase the local flame speed relative to S_L^0 (Poludnenko and Oran, 2011). The formation and destruction of flame fingers has been proposed as a mechanism of overall turbulent burning rate oscillations observed in DNS (Lipatnikov et al., 2015).

Flame-flame interactions were often observed in the present study, and an example time sequence is shown in Figure 16 for Case 1. During this time sequence, the 3D Mie-scattering flame surface topology agreed well with the OH signal in the PLIF plane, indicating that the local seeding was adequate for the 3D surface to represent the main features of the flame. The z-orientation of the measured 3D flame surface was negligible, indicating that the planar measurements are likely representative of the main flame dynamics. There is a possibility that

Fig. 13 Example of exact and tracked particle positions (z = 0.0 cm) for $S = 10^3$ s^{-1}. Contoured by x-velocity in m/s. Only centroid of tracked control mass is shown for clarity

Fig. 15 Depiction of flame speed measurement during flame-flame interaction via TLP tracking.

a small highly-curved flame feature in the z-direction occured during the presented event, which may not be detected in the 3D flame. However, these occurred over only about 4% of the flame (based on deviations on the in-plane measurements), and hence is unlikely to influence the observed results. Moreover, little z-convection occurred, as will be discussed below.

Local flame speed was measured as half the closure rate between points, which was most simply achieved using topologically obvious points on the OH contours. The effect of differential convection was accounted for by making use of the aforementioned TLP tracking, as depicted in Figure 15. TLPs were placed on the flame edge in a flame-flame interaction. These were tracked forward in time, and their separations were measured (d_{TLP}). Points on the flame edge that topologically corresponded to the initial points were identified, and the separation measured (d_{FE}). The flame speed could thus be measured as $S_L = (d_{TLP} - d_{FE})/(2\Delta t)$.

The time sequence for Case 1 in Figure 16 shows the typical formation of a flame neck through collision of two roughly parallel laminar-like flame surfaces. The flame speeds are taken using a central difference technique, and give speeds of between 66-107 cm/s, or around 2-3.5 S_L^0. Note that this only considers the x and y movement of the TLPs, as only the OH contours were used in identifying the flame surfaces. TLP movement in the z-direction in this sequence was on average 0.08 mm, well below the OH PLIF laser sheet thickness. High flame speeds occur at times in which the CH_2O regions of opposing flame surfaces have merged. Hence, the flame acceleration may be linked to a concentration of heat, increasing the local temperature and the kinetic rates that control the flame speed.

3.2.3 Residence time of fluid in the CH_2O zone

The time required for the flame to propagate its thickness is a fundamental parameter in premixed combus-

tion. Defining τ_c as the time required for the flame contour determined from the Mie scattering tomography (approximately equivalent to the heat release zone) to traverse the thickness of the CH_2O layer (approximately equivalent to the preheat zone), $\tau_c^{-1} \sim S_L/\delta_l \sim \dot{m}_f/\rho_u$, where $\dot{m}_f$ is the mass consumption rate of fuel per unit volume and ρ_u is the unburnt gas density. τ_c can equally be viewed as the time required for fluid to traverse from the leading edge of the CH_2O layer to the heat release zone. This formulation is far simpler to calculate, as it does not require a separation of the flame motion into convection and propagation components, and instead can be done via TLP tracking. Similarly, τ_c can be reviewed as the residence time of the TLPs in the CH_2O region.

For each instantaneous measurement, the upstream edge of the CH_2O region was identified and TLPs were placed along this edge. The TLPs were defined in the $z = 0$ plane only, as this is the plane containing the PLIF measurements. Each TLP was tracked forward in time until it reached the Mie scattering flame surface, which determined τ_c for that TLP. Because each TLP is able to convect in the z direction, the end condition for the TLP was based on the Mie scattering surface as oppose to the OH PLIF directly. TLPs that left the measurement volume before reaching the Mie scattering surface were disregarded from the analysis. Such residence times were calculated for Cases 1-2. It was found that for Case 3, the flow velocity was sufficiently high that it was difficult to track TLPs from the CH_2O leading edge to the heat release zone before they left the FOV.

An example of this tracking is shown in Figure 17 for Case 1, showing both an isometric and top-down view, wherein half the domain is removed for clarity. TLPs (centroids indicated by red circles) start on the leading edge of the CH_2O layer (green contour) and move through the layer with time as the flame moves relative to the fluid. The color of the circles changes from red to black as the TLPs pass through the Mie scattering surface at t = 0.6 ms. At each particle position, the nearest distance to the Mie scattering surface can be determined to examine the progression of flow through the CH_2O layer, which is shown in Figure 18 for a randomly selected subset of particle tracks. TLPs in the higher turbulence intensity Case 2 generally had a lower residence time, despite the particles often starting at a further distance from the flame than Case 1; the mean residence time for Cases 1 and 2 were approximately 0.5 ms and 0.3 ms respectively.

The validity of the analysis can be confirmed from Case 1, which lies in the laminar flamelet regime and is expected to have flamelet-like dynamics. The Case 1 results are in good agreement with the residence time
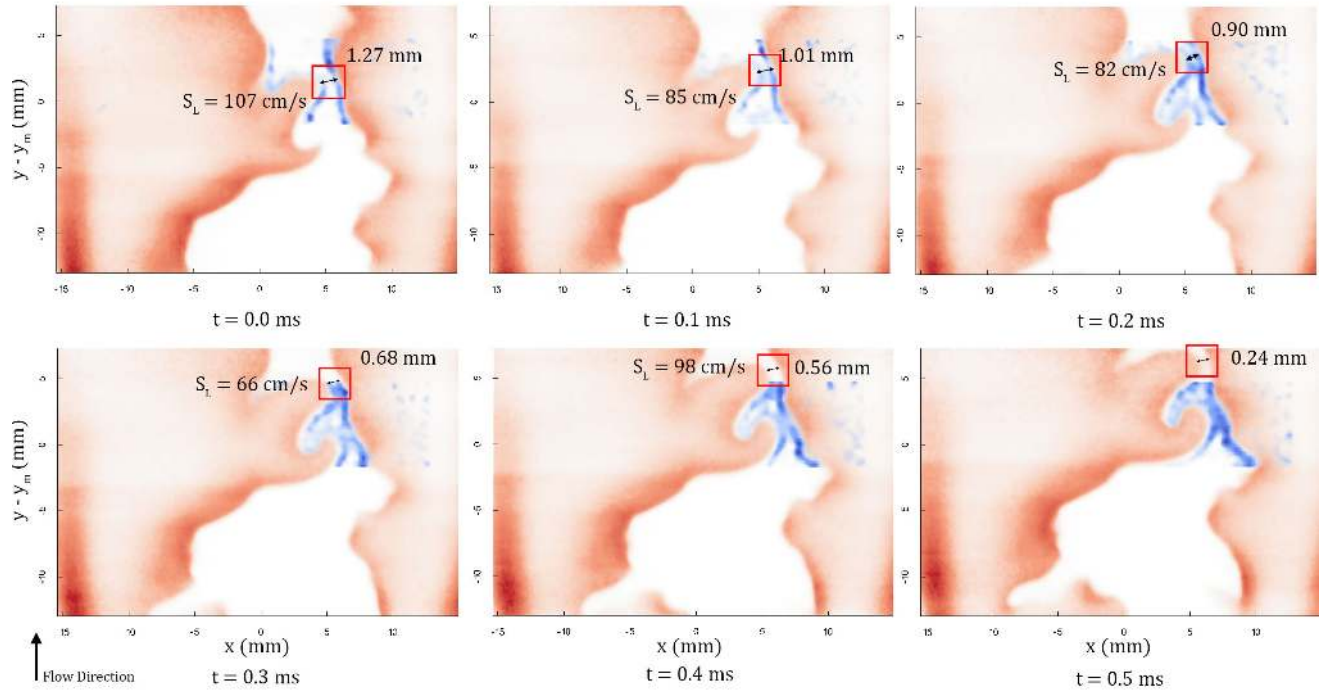
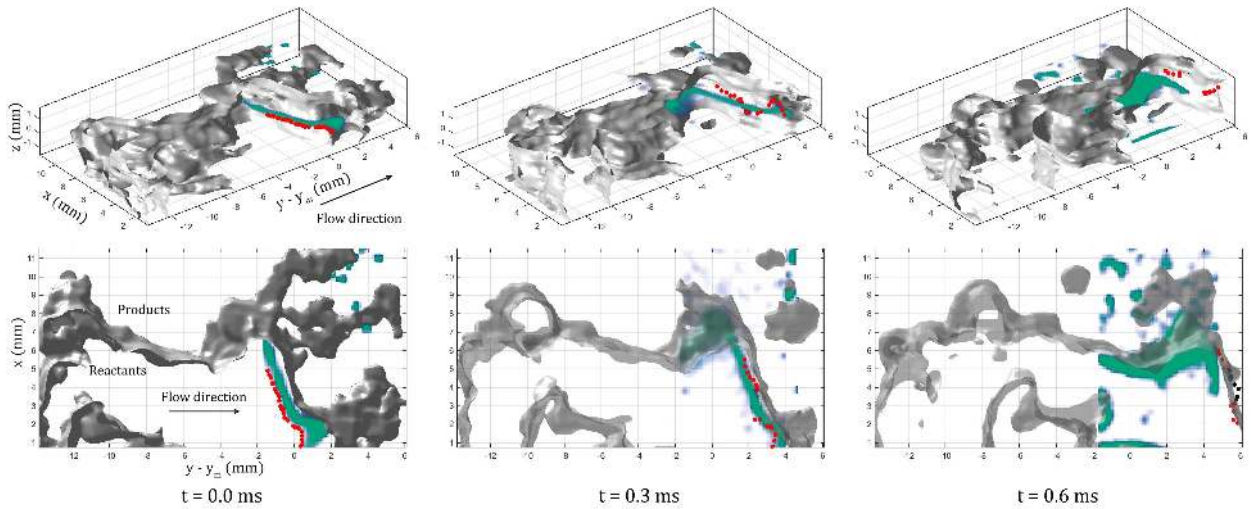**Fig. 16** Time lapse of Case 1 showing flame merging sequence

Fig. 17 Example of particle tracking through the preheat layer for Case 1. Red circles denote centroid of control masses, black circles denote control masses that have passed the flame surface, green contour is the extent of the CH$_2$O layer, and grey isosurface is the Mie scattering surface. Top and bottom images correspond to the same time steps. Transparency of 3D flame surface intentionally increased in final two frames for visibility. One in three particles shown for clarity

calculated by placing TLPs in a 1D laminar flame profile computed by Cantera using the GRIMech 3.0 chemical mechanism, which was approximately 0.6 ms. The discrepancy is likely due to the experimental uncertainty in defining the upstream and downstream boundaries over which to perform the tracking. It is noted that this time is shorter than S_L^0/δ_{CH_2O} (approximately 1.3 ms) due to acceleration through the flame.

The decrease in residence time for higher turbulence intensity flames also coincides with an increased CH$_2$O

layer thickness. This can be quantified from the minimum distance between the TLPs at the leading edge of the CH$_2$O layer and the Mie scattering surface (i.e. $d_{f,i}$ at the time each TLP is defined).

PDFs of the TLPs' initial distance to the Mie scattering surface are shown in Figure 19 for Cases 1-3, in which the statistical broadening of the flame is observed, as reported by previous authors (Skiba et al., 2015). Hence, the decrease in residence time and increase in flame thickness with increasing turbulence intensity in-
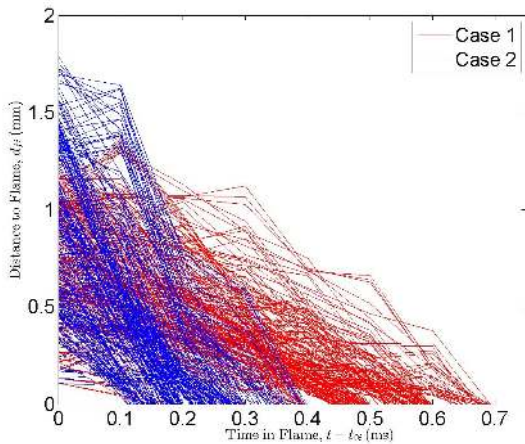
Fig. 18 Distance of TLPs to Mie scattering surface as a function of time in flame for Cases 1-2

dicates an increasing flame propagation rate. It is noted that the reported distance should not be interpreted as the actual path the TLPs follow as they traverse the flame.
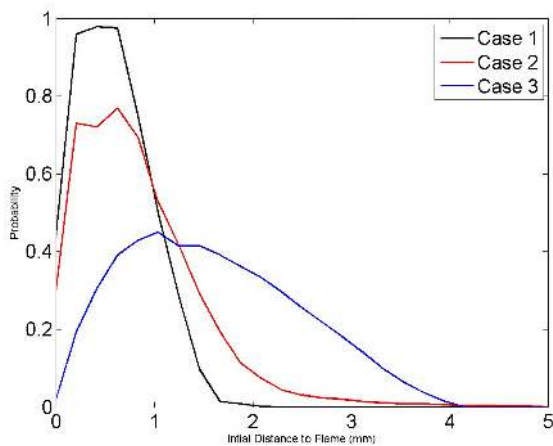

**Fig. 19** Minimum distance between initial TLP location and Mie scattering surface for Cases 1-3.

3.2.4 Turbulence evolution through the flame

This technique of TLP tracking can be used to examine the evolution of turbulence properties through the flame. Using the same particles as in Figure 18, enstrophy at each particles' location through the CH_2O layer (determined as distance to Mie scattering surface) was determined and is shown in Figure 20, showing a trend towards increasing enstrophy as the flow travels through the CH_2O layer towards the flame.

It should be noted that due to the discretization of the Mie scattering surface, the flame surface position is
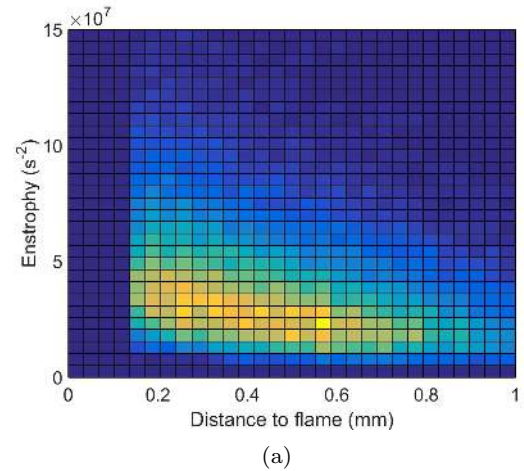
(a)
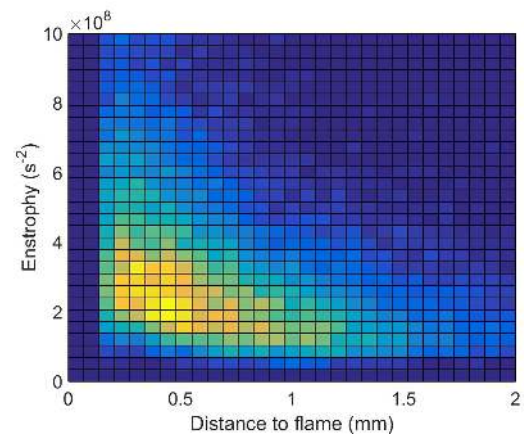
(b)

Fig. 20 Enstrophy versus distance to flame for Cases (**a-b**) 1-2. Note the different axes scaling

only known with the same accuracy as the reconstructed flame grid (i.e. 0.255 mm). It therefore is ambiguous whether particles that instantaneously exist within half this distance on either side of the flame are actually upstream or downstream. Hence, any particle that was in this range at the measurement time was removed from the analysis owing to this ambiguity. This is manifested in Figure 20 in that no particles are found at a distance to the Mie scattering surface of less than $\sim$0.128 mm.

The increase in enstrophy indicates turbulence production through the flame. Previous authors have indicated the potential significance of the baroclinic torque term in the enstrophy transport equation for turbulence generation (Poludnenko, 2014). These results support this argument, but more detailed analysis of the source terms is needed (Steinberg et al., 2015).

4 Conclusions

Simultaneous TPIV, OH, and CH$_2$O PLIF was applied at 10 kHz to a series of high turbulence intensity jet flames. Evaluation of the TPIV found that the temporal resolution was sufficient to measure all spatially-resolved flow structures, though velocity gradient calculations had some ambiguity due to noise and smoothing. A limiting factor in the scalar measurement was the CH$_2$O PLIF signal-to-noise, but this was sufficient to extract qualitative features.

Analysis of the PLIF images showed broadening of the CH$_2$O layers at elevated turbulence intensities, CH$_2$O fingers, and numerous flame-flame interactions. However, OH production remained rapid and the overlap between OH and CH$_2$O remained relatively thin. To examine the 3D structure, a method was presented for determining the 3D flame topology based on Mie scattering tomography. Comparison of the Mie scattering topology to the OH in the PLIF plane revealed that most topological features were captured. The 3D flame surfaces revealed that out-of-plane orientations were rare, and hence the structures observed in the PLIF were an accurate representation of the flame. This 3D reconstruction however was unable to capture some of the fine-scale details of the flame, and instead could only be used for general surface topology measurements.

Dynamic features were then analyzed. Flame-flame interactions exhibited increased local propagation speeds relative to the laminar flame speed, likely as a result of local preheating. A method for quantitatively tracking features of the flow was then presented based on theoretical Lagrangian particles, which were used to determine the residence time of fluid within the CH$_2$O layers and examine the evolution of turbulence through these layers. The residence time decreased with increasing turbulence intensity, indicating an increase in the local reaction rate. Enstrophy increased slightly through the CH$_2$O layer, indicating some degree of turbulence generation.

Future work will expand upon the analysis performed on flame-flame interactions, flow residence time through the CH$_2$O layer, and turbulence evolution through the flame. Of particular importance will be considering the conditional statistics of each of these processes. Such an analysis will reveal how the processes depend on the local flame and turbulence conditions. Furthermore, it will identify the underlying physical mechanisms and how these must be reflected in models.

References

Ayoola, B., Balachandran, R., Frank, J., Mastorakos, E., and Kaminski, C. Spatially resolved heat release rate measurements in turbulent premixed flames. *Combustion and Flame*, 144:1–16, 2006.

Baum, E., Peterson, B., Surmann, C., Michaelis, D., Böhm, B., and Dreizler, A. Investigation of the 3D flow field in an IC engine using tomographic PIV. *Proceedings of the Combustion Institute*, 34:2903–10, 2013.

Böckle, S., Kazenwadel, J., Kinzelmann, T., Shin, D., Schulz, C., and Wolfrum, J. Simultaneous single-shot laser-based imaging of formaldehyde, OH, and temperature in turbulent flames. *Proceedings of the Combustion Institute*, 28(1):279–286, 2000.

Boxx, I., Carter, C., and Meier, W. On the feasibility of Tomographic-PIV with low pulse-energy illumination in a lifted turbulent jet flame. *Experiments in Fluids*, 55(1771), 2014.

Brand, J. The electronic spectrum of formaldehyde. *Journal of the Chemical Society*, pages 858–72, 1956.

Buchner, A., , Buchmann, N., Kilany, K., Atkinson, C., and Soria, J. Stereoscopic and tomographic PIV of a pitching plate. *Experiments in Fluids*, 52(2):299–314, 2012.

Buschmann, A., Dinkelacker, F., Schafer, T., Schafer, M., and Wolfrum, J. Measurement of the instantaneous detailed flame structure in turbulent premixed combustion. *Proceedings of the Combustion Institute*, 26:437–45, 1996.

Chen, Y. and Bilger, R. Experimental investigation of three-dimensional flame-front structure in premixed turbulent combustion -I: Hydrocarbon/air bunsen flames. *Combustion and Flame*, 131:400–35, 2002.

Chen, Y. and Bilger, R. Experimental investigation of three-dimensional flame-front structure in premixed turbulent combustion -II: Lead hydrogen/air bunsen flames. *Combustion and Flame*, 138:155–74, 2004.

Clouthier, D. and Ramsay, D. The spectroscopy of formaldehyde and thioformaldehyde. *Annual Review of Physical Chemistry*, 34:31–58, 1983.

Coriton, B., Steinberg, A., and Frank, J. High-speed tomographic PIV and OH PLIF measurements in turbulent reactive flows. *Experiments in Fluids*, 55 (1743), 2014.

Dieke, G. and Kistiakowsky, G. The structure of the ultraviolet absorption spectrum of formaldehyde. *Physical Review Letters*, 45(4), 1934.

Donbar, J., Driscoll, J., and Carter, C. Simultaneous ch planar laser-induced fluorescence and particle imaging velocimetry in turbulent flames. *American Institute of Aeronautics and Astronautics*, 66(1), 1997.

Echekki, T. and Mastorakos, E. *Turbulent Combustion Modeling.* Springer, 2010.

Elsinga, G. and Ganapathisubramani, B. Forward: Advances in 3D velocimetry. *Measurement Science and Technology*, 24, 2012.

Elsinga, G., Scarano, F., and Wieneke, B. Tomographic particle image velocimetry. *Experiments in Fluids*, 41: 933–47, 2006.

Filatyev, S., Driscoll, J., Carter, C., and Donbar, J. Measured properties of turbulent premixed turbulent flames. *Combustion and Flame*, 141:1–21, 1998.

Floyd, J., Geipel, P., and Kempf, A. Computed tomography of chemiluminescence (CTC): Instantaneous 3D measurements and phantom studies of a turbulent opposed jet flame. *Combustion and Flame*, 2010.

Frank, J., Kalt, P., and Bilger, R. Measurements of conditional velocities in turbulent premixed flames by simultaneous OH PLIF and PIV. *Combustion and Flame*, 116:220–32, 1999.

Fukushima, N., Katayama, M., Naka, Y., Oobayashi, T., Shimura, M., and Nada, Y. Combustion regime classification of HCCI/PCCI combustion using Lagrangian fluid particle tracking. *Proceedings of the Combustion Institute*, 35(3), 2014.

Gabet, K., Patton, R., Jiang, N., Lempert, W., and Sutton, J. High-speed CH_2O plif imaging in turbulent flames using a pulse-burst laser system. *Applied Physics B*, 106(3):569–575, 2012.

Ganapathisubramani, B., Lakshimnarasimhan, K., and Clemens, N. Investigation of three-dimensional structure of fine scales in a turbulent jet by using cinematographic stereoscopic particle image velocimetry. *Journal of fluid mechanics*, 598:141–75, 2008.

Garcia, D. Robust smoothing of gridded data in one and higher dimensions with missing values. *Computational Statistics and Data Analysis*, 54:1167–78, 2010.

Goodwin, D. An open-source, extensible software suite for CVD process simulation. *In Proceedings of CVD XVI and EuroCVD Fourteen*, pages 155–62, 2003.

Humble, R., Elsinga, G., Scarano, F., and Oudheusden, B. V. Three-dimensional instantaneous structure of a shock wave/turbulence boundary layer interaction. *Journal of Fluid Mechanics*, 622:33–62, 2009.

Kuhl, J., Jovicic, G., Zigan, L., and Leipertz, A. Transient electric field response of laminar premixed flames. *Proceedings of the Combustion Institute*, 34:3003–10, 2013.

Leipertz, A., Braeuer, A., Kiefer, J., Dreizler, A., and Heeger, C. *Handbook of Combustion.* Wiley, 2010.

Li, Z., Li, B., Sun, Z., Bai, X., and Aldén, M. Turbulence and combustion interaction: High resolution local flame front structure visualization using simultaneous single-shot PLIF imaging of CH, OH, and CH_2O in a piloted premixed jet flame. *Combustion and Flame*, 157(6):1087–96, 2010.

Lipatnikov, A., Chomiak, J., Sabelnikov, V., Nishiki, S., and Hasegawa, T. Unburned mixture fingers in premixed turbulent flames. *Proceedings of the Combustion Institute*, 35:1401–8, 2015.

Moeck, J., Bourgouin, J., Durox, D., Schuller, T., and Candel, S. Tomographic reconstruction of heat release rate perturbation induced by helical modes in turbulent swirl flames. *Experiments in Fluids*, 54(1498), 2013.

Olofsson, J., Richter, M., Auge, M., and Aldén, M. Development of high temporally (MHz) and spatially (3D) resolved formaldehyde measurements in combustion environments. *Review of Scientific Instruments*, 77, 2006.

Paul, P. and Najm, H. Planar laser-induced fluorescence imaging of flame heat release rate. *Proceedings of the Combustion Institute*, 27(1):43–50, 1998.

Peterson, B., Baum, E., Böhm, B., Sick, V., and Dreizler, A. High-speed PIV and LIF imaging of temperature stratification in an internal combustion engine. *Proceedings of the Combustion Institute*, 34(2):3653–60, 2013.

Petersson, P., Olofsson, J., Brackman, C., Seyfried, H., Zetterberg, J., Richter, M., Aldén, M., Linne, M., Cheng, R., Nauert, A., Geyer, D., and Dreizler, A. Simultaneous PIV/OH-PLIF, Rayleigh thermometry/OH-PLIF and stereo PIV measurements in a low-swirl flame. *Applied Optics*, 46(19): 3928–36, 2007.

Poludnenko, A. Pulsating instability and self-acceleration of fast turbulent flames. *Physics of Fluids*, 27:014106, 2014.

Poludnenko, A. and Oran, E. The interaction of high-speed turbulence with flames: Global properties and internal flame structure. *Combustion and Flame*, 157 (2):301–26, 2010.

Poludnenko, A. and Oran, E. The interaction of high-speed turbulence with flames: Turbulent flame speed. *Combustion and Flame*, 158:301–26, 2011.

Richter, M., Collin, R., Nygren, J., Aldén, M., Hildingsson, L., and Johansson, B. Studies of the combustion process with simultaneous formaldehyde and OH PLIF in a direct-injected HCCI engine. *JSME International Journal*, 48(4):701–7, 2005.

Roy, S., Miller, J., Slipchenko, M., Hsu, P., Mance, J., Meyer, T., and Gord, J. 100-ps-pulse-duration, 100-J burst-mode laser for kHz-MHz flow diagnostics. *Optics Letters*, 39(22):6462–6465, 2014.

Scarano, F. and Poelma, C. Three-dimensional vorticity patterns of cylinder wakes. *Experiments in Fluids*, 47: 69–83, 2009.

Schroeder, A. and Willert, C. *Particle Image Velocimetry: new developments and recent applications.* Springer, 2008.

Shepherd, I. and Cheng, R. The burning rate of premixed flames in moderate and intense turbulence. *Combustion and Flame*, 127:2066–75, 2001.

Shimura, M., Ueda, T., Tanahashi, M., Choi, G., and Miyauchi, T. Simultaneous dual-plane ch plif/single-plane oh plif and dual-plane stereoscopic piv in turbulent premixed flames. *15th International Symposium on Laser Techniques to Fluid Mechanics*, 2010.

Skiba, A., Wabel, T., Temme, J., and Driscoll, J. Measurements to determine the regimes of turbulent premixed flames. In *51st AIAA/SAE/ASEE Joint Propulsion Conference*, Orlando, FL, July 2015.

Steinberg, A. and Driscoll, J. Straining and wrinkling processes during turbulence-premixed flame interaction measured using temporally-resolved diagnostics. *Combustion and Flame*, 156:2285–2306, 2009.

Steinberg, A., Driscoll, J., and Ceccio, S. Measurements of turbulent premixed flame dynamics using cinema-stereoscopic PIV. *Experiments in Fluids*, 44:985–99, 2008.

Steinberg, A., Boxx, I., Stöhr, M., Arndt, C., Meier, W., and Carter, C. Influence of flow-structure dynamics on thermo-acoustic instabilities in oscillating swirl flames. In *Joint Propulsion Conference*, San Diego CA, July 2011.

Steinberg, A., Coriton, B., and Frank, J. Influence of combustion on principal strain-rate transport in turbulent premixed flames. *Proceedings of the Combustion Institute*, 35:1287–94, 2015.

Stella, A., Guj, G., Kompenhans, J., Richard, H., and Raffel, M. Three-components particle image velocimetry measurements in premixed flames. *Aerospace Science Technology*, 5:357–64, 2001.

Temme, J., Wabel, T., Skiba, A., and Driscoll, J. Measurements of premixed turbulent combustion regimes of high reynolds number flows. *AIAA SciTech*, 2015.

Tokare, M., Sharaborin, D., Lobasov, A., Chikishev, L., Dulin, V., and Markovich, D. 3D velocity measurements in a premixed flame by tomographic PIV. *Measurement Science and Technology*, 26(064001), 2014.

Trunk, P., Boxx, I., Heeger, C., Meier, W., Böhm, B., and Dreizler, A. Premixed flame propagation in turbulent flow by means of stereoscopic PIV and dual-plane OH-PLIF at sustained kHz repetition rates. *Proceedings of the Combustion Institute*, 34:3565–72, 2013.

Wang, J., Zhang, M., Huang, Z., Kudo, T., and Kobayashi, H. Measurement of the instantaneous flame front structure of syngas turbulent premixed flames at high pressure. *Combustion and Flame*, 160:

2434–41, 2013.

Weinkauff, J., Michaelis, D., Dreizler, A., and Böhm, B. Tomographic PIV measurements in a turbulent lifted jet flame. *Experiments in Fluids*, 54(1624), 2013.

Wellander, R., Richter, M., and Aldén, M. Time-resolved (kHz) 3D imagine of OH PLIF in a flame. *Experiments in Fluids*, 55(1764), 2014.

Westerweel, J., Elsinga, G., and Adrian, R. Particle image velocimetry for complex and turbulent flows. *Annual Review of Fluid Mechanics*, 45:409–36, 2013.

Williams, F. Criteria for existence of wrinkled laminar flame structure of premixed turbulent flames. *Combustion and Flame*, 26:269–70, 1976.

Winkauff, J., Michaelis, D., Dreizler, A., and Bohm, B. Tomograpic PIV measurements in a turbulent lifted jet flame. *Experiments in Fluids*, 54(1624), 2013.

Worth, N., Nickels, T., and Swaminathan, N. A tomographic PIV resolution study based on homogeneous isotropic turbulence DNS data. *Experiments in Fluids*, 49:637–56, 2010.

Xu, W., Wickersham, A., and Ma, L. 3D flame topography obtained by tomographic chemiluminescence with direct comparison to planar scattering measurements. *Applied Optics*, 54(9):2174–82, 2015.

Yeung, P. and Pope, S. An algorithm for tracking fluid particles in numerical simulations of homogeneous turbulence. *Journal of Computational Physics*, 79: 373–416, 1988.

Zhou, B., Kiefer, J., Zetterberg, J., Li, Z., and Aldén, M. Strategy for PLIF single-shot HCO imaging in turbulent methane/air flames. *Combustion and Flame*, 161:1566–74, 2014.
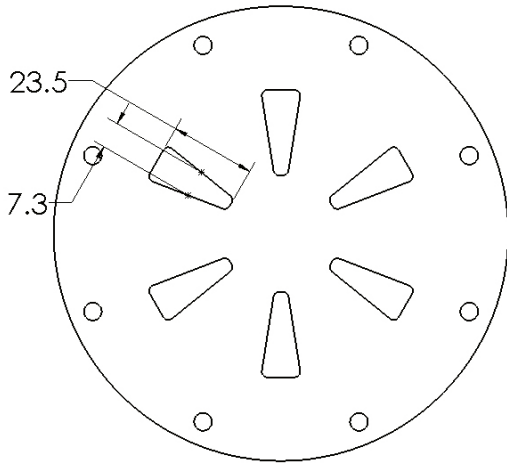
Appendix

Burner Geometry

Two perforated plates were used to generate isotropic turbulence in the Hi-Pilot burner, as was shown in Figure 1b. The geometry of the turbulence generating plates are shown in Figure 21

Hi-Pilot Jet Boundary Conditions

Hot wire measurements were performed at the jet exit plane in order to characterize the boundary conditions. Contours of exit plane velocity and mean velocity fluctuations $u_t' = \overline{|u - \overline{u}|}$ are shown in Figure 23. As can be seen, there was a slight asymmetry in the velocity fluctuations profile, which was believe to be caused by manufacturing imperfections. Raw exit plane velocity data can be made available upon request.
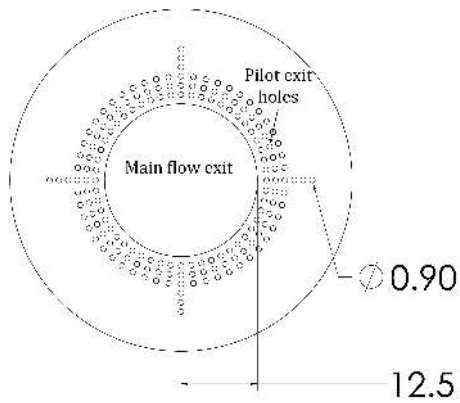
(a)

(a) Mean velocity (m/s)

(b) Velocity fluctuations (m/s)
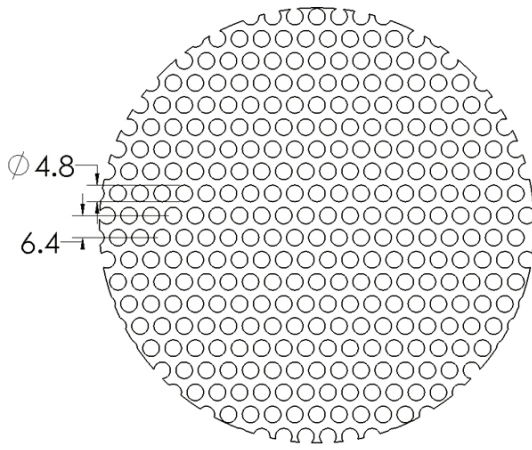
Fig. 23 Velocity statistics at jet exit plane for Cases 1-3 (left to right) from CTA
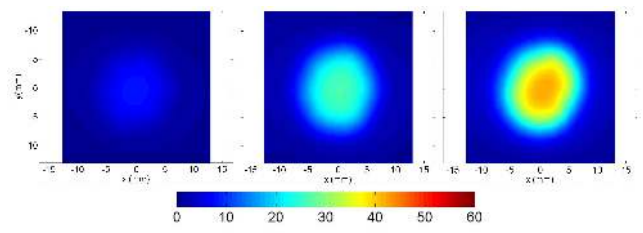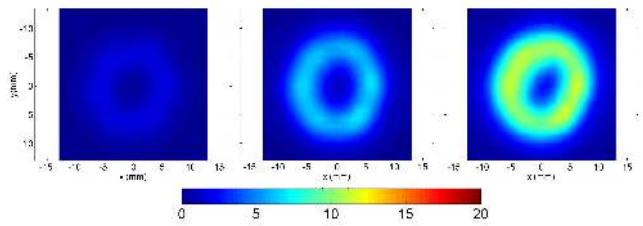

(b)

Fig. 21 Geometry of **a** turbulence plate A and **b** B. Dimensions in mm and percent open area is respectively 51% and 15%

Fig. 22 Plane view of the pilot exit plate, dimensions in mm.